Efficient WO$_{3-x}$ nanoplates photoanode based on bidentate hydrogen bonds and thermal reduction of ethylene glycol

Jiachen Wang [a],[1], Yan Zhang [a],[1], Tingsheng Zhou [a], Shuai Chen [a], Hong Zhu [b],**, Jing Bai [a],[c], Jinhua Li [a], Baoxue Zhou [a],[c],[d],*

[a] School of Environmental Science and Engineering, Shanghai Jiao Tong University, No. 800, Dongchuan Rd, Shanghai 200240, PR China
[b] University of Michigan – Shanghai Jiao Tong University Joint Institute, Shanghai Jiao Tong University, Shanghai 200240, PR China
[c] Shanghai Institute of Pollution Control and Ecological Security, Shanghai 200092, PR China
[d] Key Laboratory of Thin Film and Microfabrication Technology, Ministry of Education, Shanghai 200240, PR China

ARTICLE INFO

ABSTRACT

In this study, an efficient WO$_{3-x}$ nanoplates photoanode was generated based on bidentate hydrogen bonds and in subsequent thermal reduction of ethylene glycol (EG). An appropriate number of controllable oxygen vacancies (O$_v$) was generated in-situ on the surface of the WO$_3$ nanoplates without deep defects by bidentate hydrogen bonds. Density functional theory (DFT) calculations indicate that the distance between two alcoholic hydrogens (5.124 Å) in EG matches that of the diagonal oxygens (5.483 Å) in the WO$_3$ (0 0 2) surface, which allows EG to combine through the most stable bidentate hydrogen bonds with O–H intervals of approximately 2.5 Å. Diagonal oxygens are captured directly from the surface, leaving O$_v$ owing to the special hydrogen-bond structure and moderate reducibility of EG under appropriate thermal conditions. The photocurrent density of the WO$_{3-x}$ nanoplates improves considerably to 2.07 from the 0.91 mA cm^{-2} of pristine WO$_3$ with the introduction of O$_v$, which demonstrates the superior surface reaction kinetics from the reduced holes-to-water resistance and increase in surface injection efficiency. DFT calculations of the oxygen evolution reaction reveal that surface O$_v$ could substantially decrease the reaction energy barrier for a lower overpotential of 0.494 V compared to that of WO$_3$ (1.037 V), which is consistent with the reduction in the Tafel slope from 412 to 243 mV dec^{-1}. Therefore, this study provides an innovative method to obtain an efficient WO$_3$ photoanode based on the treatment of EG.

1. Introduction

Photoelectrocatalytic (PEC) water splitting for H$_2$ generation is one of the most promising strategies for converting abundant solar power and realizing sustainable energy storage [1]. A considerable number of studies have been performed to develop various semiconductors (e.g., Fe$_2$O$_3$ [3,4], BiVO$_4$ [5,6], and ZnO [7,8]) for photoanodes, since solar water splitting was proposed in the 1970s [2]. WO$_3$ is recognized as a potential photoanode material among all transition metal oxides because of its suitable band gap and band edge, excellent electron transfer, long hole lifetimes, and chemical stability in acidic aqueous solutions [9–13]. Nevertheless, the PEC performance of WO$_3$ is substantially restricted by slow interface hole transfer, fast charge-carrier recombination, and sluggish kinetics [10,14,15].

Herein, WO$_{3-x}$ nanoplates with efficient interfacial charge transfer and superior surface reaction kinetics were obtained based on bidentate hydrogen bonds and the subsequent thermal reduction of ethylene glycol (EG). An appropriate number of controllable oxygen vacancies (O$_v$) was generated in-situ on WO$_{3-x}$ nanoplates surface. O$_v$ engineering has been effective at ameliorating the optical and electronic properties of semiconductor photoanodes to enhance water oxidation [16], which can promote solar light harvesting [17,18], increase the charge carrier densities by decreasing the of band gap [19,20], and dissociate water molecules as active sites [21,22].

However, the traditional methods for creating O$_v$ in WO$_3$, such as annealing in H$_2$, which is the most common method [23], can extend O$_v$ from the surface to the bulk region, introducing deep defects owing to its strong reducibility. The O$_v$ in bulk may act as recombination centers and

---

decrease the electron mobility, which harms the PEC performance [24,25]. In contrast, the O_v on the WO_3 surface can adsorb water as reactive sites and improve interfacial charge transfer with enhanced surface catalysis [26]. Therefore, modulating O_v on WO_3 without creating deep defects is a key issue.

In this paper, we reduced pristine WO_3 by bidentate hydrogen bonds between EG and diagonal oxygens of WO_3 to construct O_v on the surface rather than the bulk. The obtained WO_{3-x} nanoplates photoanode had a significantly improved photocurrent density, increasing from 0.91 to 2.07 mA cm^{-2} at 1.23 V vs. reversible hydrogen electrode (RHE). Density functional theory (DFT) calculations indicate that the distance between two alcoholic hydrogens (5.124 Å) in EG matches that of the diagonal oxygens (5.483 Å) in WO_3 (0 0 2) surface forming bidentate hydrogen bonds to capture surface oxygen atoms under thermal reduction. And DFT also revealed that surface O_v could lower the energy barrier of the oxygen evolution reaction (OER) with the overpotential decreasing from 1.037 to 0.494 V, which is consistent with the reduction in the Tafel slope from 412 to 243 mV dec^{-1}. Therefore, thermal reduction by EG can introduce O_v in the WO_3 nanoplates surface, while avoiding the creation of structural defects (bulk O_v), and WO_{3-x} can improve the PEC performance for rapid interfacial charge transfer.

2. Experimental

2.1. Synthesis of WO₃ and WO₃₋ₓ nanoplates

WO_3 nanoplates were hydrothermally grown on fluorine-doped tin oxide (FTO) glass substrate [12]. Initially, 1.0 g of ammonium *para*-tungstate $[(NH_4)_{10}(H_2W_{12}O_{42}) \bullet 4H_2O]$ was dissolved in 93 mL of deionized water and stirred for 1 h. Subsequently 2 mL of HCl (37%) and 4 mL of H_2O_2 (30%) were added and stirred for 1 h, respectively, to get transparent and clear solution. Afterwards the cleaned and faced down FTO was placed inside the Teflon-liner autoclave and reacted at 160 °C for 4 h. The hydrothermally synthesized films were annealed at 500 °C for 2 h to convert into crystalline WO_3.

The WO_{3-x} nanoplates photoanode was prepared via a facile and moderate thermal reduction by EG. The obtained WO_3 substrate was immersed into pure EG (>99%) in a 30 mL reaction kettle, and reduced at 130 °C for 10 h to introduce controllable O_v by bidentate hydrogen bonds. The film was rinsed with deionized water repeatedly and dried in a vacuum oven at 50 °C for 1 h after the reactor cooled to room temperature. The resulting WO_{3-x} electrode with the introduction of O_v was used for the following experiments.

2.2. Material characterization

The morphologies were investigated by field emission scanning electron microscopy (FE-SEM; Ultra Plus, Zeiss, Germany) with an accelerating voltage of 5 kV. The microstructure was determined by high-resolution transmission electron microscopy (HRTEM; Tecnai G2 F30 S-TWIN, FEI, USA). X-ray diffraction (XRD) patterns were recorded on X-ray diffractometer (XRD; AXS-8 Advance, Bruker, Germany). Raman spectra were obtained using a LabRAM ARAMIS Raman system, exciting two wavelength lasers of 532 nm and 325 nm to characterize the position of O_v. X-ray photoelectron spectrometry (XPS; AXIS UltraDLD, Kratos, Japan) and XPS etching spectrometry were performed to reflect the amount of O_v at the surface and the bulk. Fourier transform infrared (FT-IR) spectroscopy were performed using IR/Nicolet 6700 (Thermo Fisher, America). Electron paramagnetic resonance (EPR) signals were obtained on a Bruker E500 EPR spectrometer at room temperature. Ultraviolet–visible diffuse reflectance spectra (UV–Vis DRS) were investigated by a UV–vis spectrophotometer (TU1900, Beijing Purkinje General Instrument Co. China).

2.3. PEC measurements

PEC measurements were obtained using a standard three-electrode cell, which included a Ag/AgCl electrode as the reference electrode, a Pt cathode as the counter electrode, and the as-prepared films as the working electrode. The electrolyte was a 0.2 M Na_2SO_4 aqueous solution, and the test was performed on an electrochemical workstation (CHI 660d, CH Instruments Inc., Shanghai). A 300 W Xenon lamp (PLS-SXE300) coupled with an AM 1.5G solar power system was used as an illumination source with a light instability of less than ±6% (10 h), and a centralized digital power management control mode based on a micro CPU. Photocurrent density–potential (*J–V*) curves were measured at a scan rate of 50 mV s^{-1} by linear sweep voltammetry (LSV), and the chopped *J–V* curves were recorded by chopped light voltammetry (CLV). The applied bias vs. RHE (E_{RHE}) was calculated according to Eq. (1):

$$E \text{ (RHE)} = E \text{ (Ag/AgCl)} + E_{\text{(Ag/AgCl)}} \text{ (reference)} + 0.0591\ V \times pH, \quad (1)$$

where $E_{Ag/AgCl}$ is the applied bias vs. Ag/AgCl and $E_{Ag/AgCl}$ (reference) is the standard electrode potential of the Ag/AgCl electrode (0.1976 V at 25 °C).

The incident photon-to-current efficiency (IPCE) was measured using a system comprising a monochromator (Zolix, China), a 500 W xenon arc lamp, a calibrated silicon photodetector and power meter with monochromatic light irradiation. The IPCE was calculated using Eq. (2):

$$IPCE\ (\%) = (1240 \times J_{\text{mono}})/(P_{\text{mono}} \times \lambda) \quad (2)$$

where J_{mono} is the measured photocurrent density at a specific wavelength, P_{mono} is the measure irradiance at a specific wavelength, and λ is the wavelength of the incident light.

The applied bias photon-to-current conversion efficiency (ABPE) of the films was computed using Eq. (3):

$$ABPE\ (\%) = (J \times (1.23 - V_b)/P_{\text{tot}}) \times 100\%, \quad (3)$$

where J is the photocurrent density at the applied bias (mA cm^{-2}), V_b is the applied bias (V vs. RHE), and P_{tot} is the power density of the incident light (mW cm^{-1}).

Electrochemical impedance spectroscopy (EIS) was measured with AC frequencies from 100 kHz to 0.1 Hz, under irradiation at 1.23 V vs. RHE. Mott-Schottky (MS) plots were measured at a frequency of 1 kHz, with DC voltages from 0.2 to 1.4 V.

The charge carrier density (N_d) was obtained using Eq. (4) [27]:

$$N_d = (2/e\varepsilon_0\varepsilon) \times [d(1/C^2)/dV]^{-1}, \quad (4)$$

where C is the space charge capacitance in the semiconductor, e is the elementary charge value, ε_0 is the permittivity of vacuum, ε is the relative permittivity of the semiconductor, and V is the applied potential.

2.4. Computational methods

Computational results were calculated using the Vienna Ab Initio Simulation Package (VASP), with the ion-electron interaction computed by the projector-augmented wave (PAW) method [28,29]. The exchange-correlation potential was simulated with the Perdew-Burk-Ernzerhof (PBE) function [30]. Additionally, the Hubbard model (DFT + U approach) was used for the correlation corrections, and the correlation energy was fixed at 6.2 eV for the 4f orbital of W [31]. The Kohn-Sham equations were self-consistent, solved by three-dimensional (3D) periodic boundary conditions with energy tolerance of 10^{-5} eV. Gamma-centered k-space grid 3 × 3 × 3 and 3 × 3 × 1 were used for the monoclinic phase and slab model, respectively, with 520 eV as the energy cutoff. The atom positions and vectors were optimized to achieve a calculated atomic force of < 0.01 eV Å^{-1} on each atom in the slabs.

Water oxidation involves four proton-coupled electron transfer steps with the OER on the anode as follows:
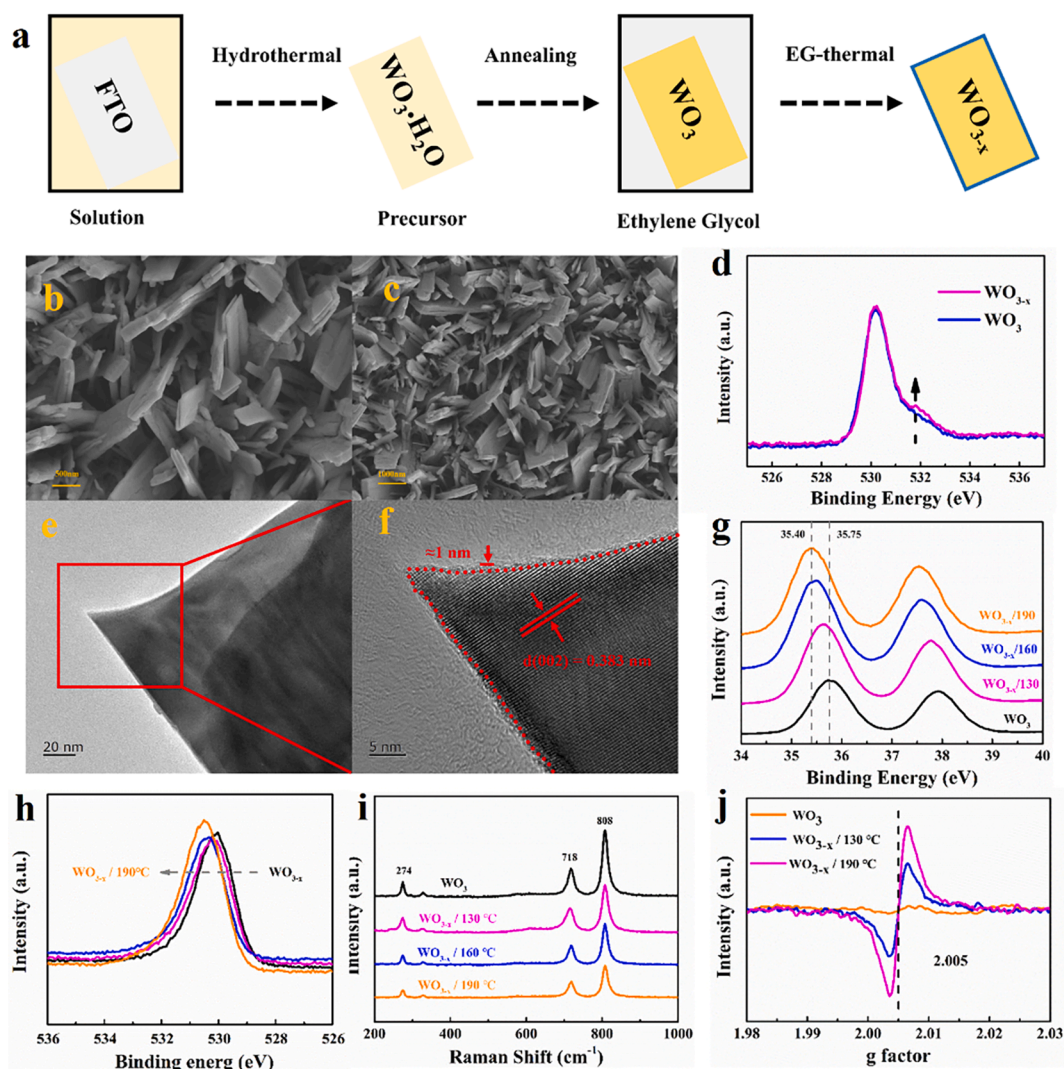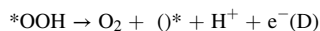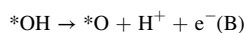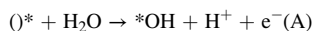
Fig. 1. (a) Schematic of WO$_{3-x}$ fabrication by thermal reduction of EG; (b-c) SEM images of WO$_{3-x}$; (d) total O 1 s XPS spectra of WO$_3$ and WO$_{3-x}$/130 °C; (e-f) HRTEM images of WO$_{3-x}$; (g-i) W 4f XPS spectra, O 1 s XPS spectra at a depth of approximately 50 nm and Raman spectra of WO$_3$ and WO$_{3-x}$ at 130, 160, and 190 °C; (j) EPR spectra of WO$_3$ and WO$_{3-x}$ at 130 and 190 °C.

$$()* + H_2O \rightarrow *OH + H^+ + e^- \quad (A)$$

$$*OH \rightarrow *O + H^+ + e^- \quad (B)$$

$$*O + H_2O \rightarrow *OOH + H^+ + e^- \quad (C)$$

$$*OOH \rightarrow O_2 + ()* + H^+ + e^- \quad (D)$$

where ()* indicates an active surface site (i.e., an undercoordinated surface W atom) and A, B, C and D label the reaction steps [32].

The reaction Gibbs free energy changes (ΔG) were adopted to evaluate the OER performance of each step using Eq. (5):

$$\Delta G\ (U, pH) = \Delta E + \Delta ZPE - T\Delta S - eU - k_B T \ln 10 * pH \quad (5)$$

where ΔE is obtained directly from DFT calculations, ΔZPE is the change in the zero-point energies (ZPEs), T is the temperature (298.15 K), and ΔS is the change in the entropy of products and reactants, and *U* is the external applied bias.

3. Results and discussions

3.1. Structural characterization of the photoanodes

Fig. 1a illustrates the preparation of WO$_{3-x}$ nanoplates on FTO substrates, where orthorhombic WO$_3$·0.33H$_2$O precursors grew hydrothermally. WO$_3$·0.33H$_2$O samples were transformed into hexagonal WO$_3$ nanoplates in wax yellow by annealing at 500 °C for 2 h in air. Subsequently, the O$_v$ photoanode of WO$_{3-x}$ was obtained via a thermal reduction of EG at 130 °C for 10 h, which is the optimal reaction condition according to the photocurrent density in Table S1–S2. The light yellow WO$_{3-x}$ that formed at 130 °C introduced more controllable O$_v$ into the structure under moderate reaction conditions (Figure S1), compared to the olive-green sample that formed at 190 °C with a lower photocurrent density, owing to bulk O$_v$, which may promote visible light harvesting (Figure S2) but act as hole-and-electron recombination centers [24]. The long reduction time (15 h) may produce excess O$_v$ to decrease the photocurrent density for the lower slope in Figure S3 with higher carrier density [19,20]. The SEM images (Fig. 1b-c) of WO$_{3-x}$ display vertical rectangular (3D) nanoplates with a thickness of ~10 nm, and WO$_3$ nanoplates with the same morphology are shown in Figure S4. The XRD patterns (Figure S5) illustrate three sharp peaks located at 23.1°, 23.5°, and 24.3° for WO$_3$ and WO$_{3-x}$/130 °C that correspond to a

Table 1
FWHM of primary Raman shifts under 532 nm excitation.

Sample	FWHM around 808 cm^{-1}
WO$_3$	16.54 cm^{-1}
WO$_3$/130 °C	16.90 cm^{-1}
WO$_3$/160 °C	18.66 cm^{-1}
WO$_3$/190 °C	20.34 cm^{-1}

monoclinic structure (PDF#43-1035) with negligible discrepancies in crystal phases. The total O 1 s XPS spectrum of WO$_{3-x}$/130 °C in Fig. 1d has an intensified signal at 531.5 eV corresponding to O$_v$ states [24], which is confirmed by the deconvoluted O 1 s XPS spectra (Figure S6). A lattice-disordered layer of approximately 1 nm thickness can be seen in the HRTEM images of WO$_{3-x}$/130 °C (Fig. 1e-f), where oxygens may leave the surface to form Ov [33], and the interplanar distance of 0.383 nm corresponds to the exposed (0 0 2) surface.

The W 4f XPS spectra of WO$_3$ and WO$_{3-x}$ samples are shown in Fig. 1g. The characteristic peaks for WO$_{3-x}$ shifted to lower binding energies as the temperature increased (from 35.75 eV for WO$_3$ to 35.40 eV for WO$_{3-x}$/190 °C), suggesting a gradual increase in the presence of W^{5+} with an increase in the O$_v$ amount [34,35]. Fig. 1h shows the O 1 s XPS spectra at a depth of approximately 50 nm, which could reflect the bulk oxygen species in the photoanodes [36]. The binding energy shifted to higher values with increasing temperature, which is attributed to an increasing amount of bulk O$_v$ [37], and the peak position of WO$_{3-x}$/130 °C was close to that of WO$_3$ for a similar amount of bulk O$_v$. Fig. 1i, illustrates the Raman spectra under 532 nm excitation, which have three characteristic peaks: 274, 718, and 808 cm^{-1}; they are attributed to the bending vibration of δ(O-W-O) and stretching vibration of ν(W-O-W), which are in agreement with that of monoclinic WO$_3$ [38]. The Raman intensities gradually decreased as the temperature increased, indicating that the W coordination environment changed and the amount of O$_v$ could be modulated by temperature [25,35,37]. The full width half maximum (FWHM) of the 532 nm Raman band around 808 cm^{-1} shown in Table 1, reflects the amount of bulk O$_v$ [24,39] and the similar FWHMs of WO$_3$ and WO$_{3-x}$/130 °C indicates that few bulk O$_v$ were introduced by EG at 130 °C. Figure S7 illustrates the UV Raman spectra (325 nm excitation) to characterize the surface information of the samples [40]; the results indicate that WO$_{3-x}$/130 °C generated more surface O$_v$ than WO$_3$ because of its larger FWHM. The EPR signal of WO$_{3-x}$/190 °C was much stronger than those of WO$_3$ and WO$_{3-x}$/130 °C around 2.005 (g factor) as shown in Fig. 1j, indicating that more un-paired electrons were captured by O$_v$ with temperature increasing [41,42]. The overall characterizations indicate that thermal reduction by EG has controllably introduced an appropriate amount of O$_v$ onto the WO$_3$ surface, avoiding the deep defects of bulk O$_v$ in the structure. WO$_{3-x}$/130 °C had the best PEC performance and is denoted as WO$_{3-x}$

in the subsequent discussions.

3.2. The model of bidentate hydrogen bonds

The generation of O$_v$ via thermal reduction by EG could be attributed to the moderate reducibility and chemisorption on the WO$_3$ surface, because of the hydrogen bonding based on DFT calculations. A (1 × 1) WO$_3$ slab was cleaved along the (0 0 2) plane, and a 15 Å vacuum layer was added to isolate periodic interactions (Figure S8). The stable surface of WO$_3$ was fully terminated with oxygens for annealing in air with a distance of 5.483 Å between diagonal oxygens, as shown in Fig. 2a. A reasonable EG molecule was obtained as shown in Fig. 2b with two alcoholic hydrogens 5.124 Å apart from each other. Therefore, EG alcoholic hydrogens conjugated with diagonal oxygens through bidentate hydrogen bonds by the matched distances. The EG molecule was horizontally adsorbed on the WO$_3$ surface in the most stable pattern, as shown in the inset of Fig. 2c compared to the other modes (Table S3). The adsorption energy is calculated as $E_{ad} = E_{total} - E_{surf} - E_{EG}$, where E_{total} is the total energy of binding EG and WO$_3$, E_{surf} is the energy of the O-terminated surface and E_{EG} is the energy of the EG molecule. The minimum adsorption energy of −0.728 eV at an O–H distance of 2.5 Å, signifies strong chemisorption [43]. Therefore, the alcoholic hydrogens in the EG connect with the diagonal oxygens on the WO$_3$ surface through two concomitant hydrogen bonds.

Fig. 2d illustrate the FT-IR spectra, which were used to detect the functional groups of EG (at 1042 and 1085 cm^{-1} [44,45]) and WO$_3$ (at approximately 800 cm^{-1} [35]). The WO$_{3-x}$ sample had three characteristic peaks of EG and WO$_3$, after the thermal reduction by EG, and another absorbance peak at approximately 1160 cm^{-1} which corresponds to glyoxal [46]. It is assumed that, under appropriate thermal conditions, EG was adsorbed onto the surface of WO$_3$, through bidentate hydrogen bonds between two alcoholic hydrogens in EG and the lattice oxygen in WO$_3$, to generate H$_2$O, O$_v$ and glyoxal and leave under-coordinated W (Figure S9). Because of the mismatch with lattice oxygens in WO$_3$ next layer, the EG could controllably take the surface oxygens without forming deep defects, which were inevitably introduced in the oxygen-deficient atmosphere in previous works [20,23,34].

3.3. Photo-response performance

PEC water splitting measurements were performed using a three-electrode electrochemical system, with 0.2 M Na$_2$SO$_4$ as the electrolyte under 100 mW cm^{-2} irradiation and with test bench in Figure S10. To exclude the possibility of EG being a sacrificial agent, LSV measurements of WO$_3$ were performed in different volumes of EG to compare with the photoanode immersed in EG (Figure S11); the results indicate that residual EG on WO$_3$ after reduction and drying does not
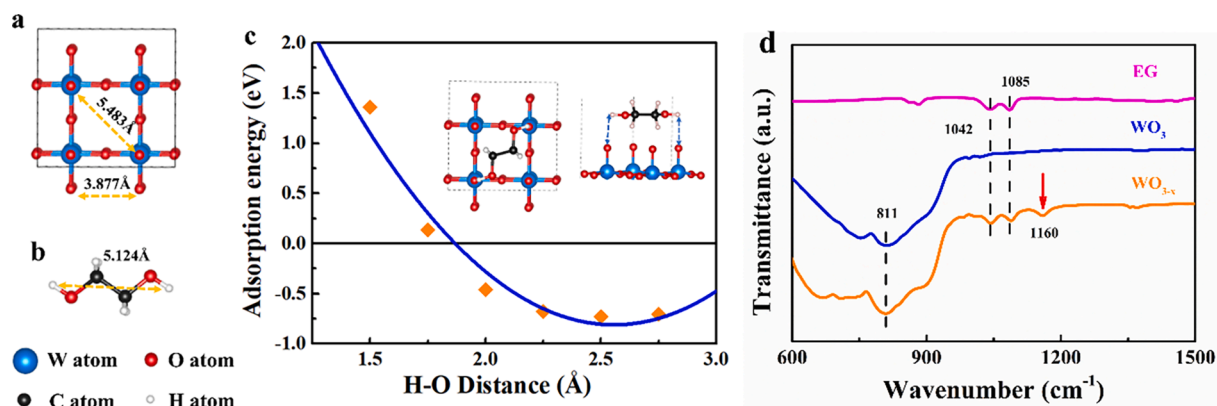

Fig. 2. (a) Top view of the O-terminated WO$_3$ surface; (b) structure of an EG molecule; (c) energy, top view, and side view of an EG molecule adsorbed by the WO$_3$ surface; and (d) FT-IR spectra of EG, WO$_3$, and WO$_{3-x}$ after thermal reduction.
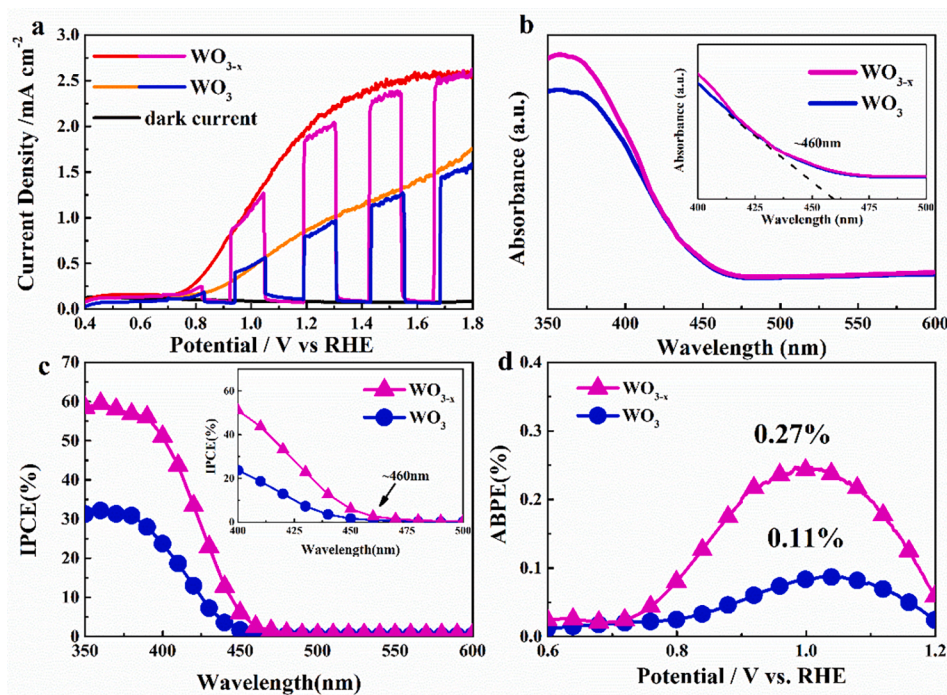
Fig. 3. (a) *J-V* curves; (b) UV–vis absorption spectra; (c) IPCE curves at 1.23 V vs. RHE; and (d) ABPE curves of WO_3 and WO_{3-x}.
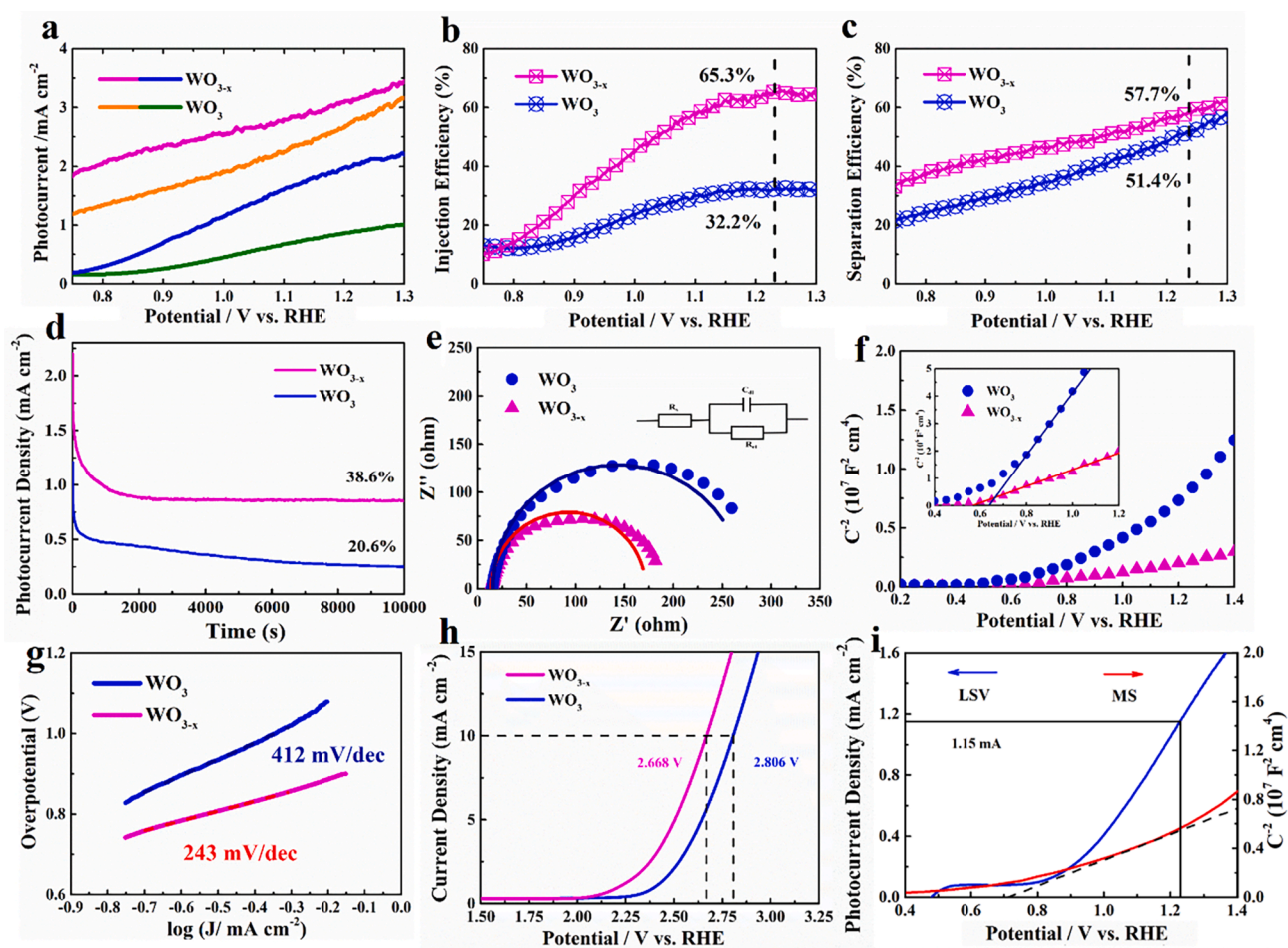

Fig. 4. (a) *J-V* curves with/without 1 M Na_2SO_3; (b-c) charge injection and separation efficiencies ($\eta_{surface}$ and η_{bulk}), respectively; (d) *I–t* curves collected at 1.23 V vs. RHE for 10000 s; (e) Nyquist and fitting plots of EIS; (f) MS plots for WO_3 and WO_{3-x}; (g-h) Tafel curves and LSV curves without irradiation, respectively, for WO_3 and WO_{3-x}; and (i) *J-V* and MS plots of WO_{3-x} after annealing in air for 1 h.
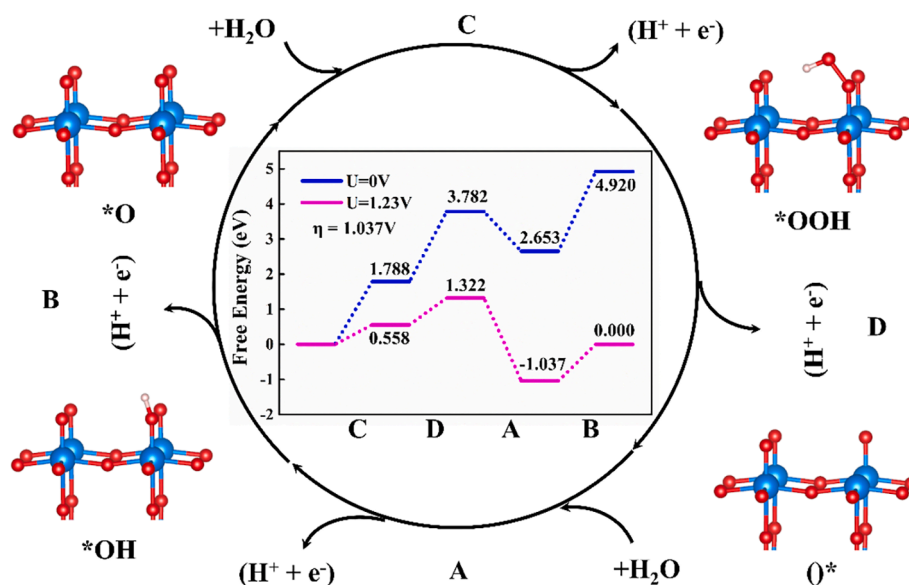
Fig. 5. OER and cumulative reaction energies on the WO$_3$ surface terminated with oxygens.

increase the photocurrent density significantly. The photocurrent density-potential (*J–V*) curves in Fig. 3a, reveal that WO$_{3−x}$ exhibited a 2.07 mA cm^{-2} photocurrent density at 1.23 V vs. RHE which was reproducible with three repeated samples (Figure S12), 2.27 times higher than the 0.91 mA cm^{-2} exhibited by WO$_3$. The obtained photocurrent density of 2.07 mA cm^{-2} is higher than those of WO$_3$ based materials with O$_v$ introduced by other state-of-the-art methods (Table S4). To prove that the O$_v$ are responsible for the improved PEC performance rather than the EG, another method of producing O$_v$ in WO$_3$ that used ascorbic acid [19] was performed for comparison which yielded a photocurrent density of 1.58 mA cm^{-2} (Figure S13). The CLV curves for both photoanodes (Fig. 3a) had negligible transient spikes when the light switched on (positive spikes) or off (negative spikes). These photocurrent transients suggest that holes transferred to oxidize water at the semiconductor/electrolyte interface, rather than accumulate on the trap states, which may promote recombination [47,48]. The UV–Vis DRS spectra (Fig. 3b), displayed similar trends between the two photoanodes, indicating that the enhanced photocurrent density does not derive from intensified light absorption.

The wavelength-dependent IPCEs of WO$_3$ and WO$_{3−x}$ are shown in Fig. 3c, which are based on the *J-V* curves and UV–Vis DRS spectra from 350 to 460 nm, corresponding to the band gap of 2.7 eV for WO$_3$. The IPCE of WO$_{3−x}$ is twice that of WO$_3$ at 350 nm, suggesting that O$_v$ facilitates the conversion of absorbed photons to photocurrent and improve the utilization efficiency of charge carriers. The ABPE curves demonstrate that the maximum efficiency increased from 0.11% to 0.27% with the introduction of O$_v$.

3.4. Photo- and electro- chemical analysis

To further investigate the improved PEC performance of WO$_{3−x}$, the photocurrent density (J_{PEC}) was calculated as Eq. (6) [49,50]

$$J_{PEC} = J_{abs} \times \eta_{bulk} \times \eta_{surface} \qquad (6)$$

where J_{PEC} is measured under 0.2 M Na$_2$SO$_4$, J_{abs} is estimated with 100% conversion of absorbed photons to current density, η_{bulk} is the bulk charge separation efficiency and $\eta_{surface}$ is the interface charge injection efficiency. Photogenerated holes arrive at the surface to oxidize water and suppress surface recombination ($\eta_{surface} = 100\%$) in the presence of hole scavenger (1 M Na$_2$SO$_3$). Therefore it can be expressed as $\eta_{surface} \approx J_{PEC}/J_{Na2SO3}$ and $\eta_{bulk} \approx J_{Na2SO3}/J_{abs}$ using the current curves in Fig. 4a [51]. $\eta_{surface}$ improved from 32.2% to 65.3% with the introduction of O$_v$

(Fig. 4b), whereas η_{bulk} exhibited a slight increase from 51.4% to 57.7% (Fig. 4c). The doubling of $\eta_{surface}$ is attributed to the photogenerated holes that transferred to the semiconductor/electrolyte interface directly participating in water oxidation and overcoming the surface hole-and-electron recombination. Therefore, surface O$_v$ may act as reactive sites for water oxidation immediately after holes migrate to the surface. The increase in η_{bulk} and the lower phase value in the Bode plots (Figure S14) at 1.23 V reflect the less-capacitive behavior of WO$_{3−x}$ [52], indicating that separated charges were not accumulated in the bulk with no additional deep defects introduced for creating O$_v$.

WO$_{3−x}$ had better photostability, with a higher photocurrent density retention (38.6%) higher than that of WO$_3$ (20.6%) after 10000 s as shown in Fig. 4d [23]. After 10000 s test, the XPS and EPR observation (Figure S15) could indicate that the structure of O$_v$ was stable. EIS measurements were implemented to explore the effect of controllable O$_v$ on carrier transfer kinetics. The Nyquist plots for both photoanodes in Fig. 4e contain one semicircle relative to the interfacial charge transfer. The equivalent circuit model (inset of Fig. 4e) is fitted by ZSimpWin, where R$_s$ is the systemic series resistance, R$_{ct}$ is the interfacial charge transfer resistance, and C$_{dl}$ is the capacitance of the double layer. R$_{ct}$ of WO$_{3−x}$ was fitted to (Table S5) a smaller value (158.1 Ω) than that of WO$_3$ (257.2 Ω), suggesting a lower holes-to-water resistance and better water oxidation kinetics [53,54]. The MS plots in Fig. 4f have positive slopes, indicating that WO$_3$ and WO$_{3−x}$ were n-type semiconductors and the flat-band potential shifted slightly negative for O$_v$ introducing [19,20]. Using Eq. (4), the calculated carrier density is ~2.31 × 10^{22} cm^{-3} for WO$_{3−x}$ 3.8 times over ~6.15 × 10^{21} cm^{-3} of WO$_3$. This suggests that more carriers transfer to the WO$_{3−x}$ surface participating in the oxidation of water molecules compared to WO$_3$.

The Tafel slope of WO$_{3−x}$ (243 mV dec^{-1}) is much smaller than that of WO$_3$ (412 mV dec^{-1}) in Fig. 4g, implying a significant reduction in the overpotential facilitating surface kinetics. The LSV curves of WO$_3$ and WO$_{3−x}$ under no irradiation were recorded to reflect the electrocatalyic OER performance with a 138 mV cathodic shift at 10 mA cm^{-2} for WO$_{3−x}$ (Fig. 4h), consistent with the Tafel plots. To confirm the role of surface O$_v$ on the PEC performance, the WO$_{3−x}$ sample was annealed in air at 500 °C for 1 h to fill the surface O$_v$ without changing the bulk structure [55]. It is clear that the amount of O$_v$ has decreased from the XPS and EPR (Figure S16) for 1 h air annealing consistent with the MS plot. The LSV of the reannealed sample decreased significantly to 1.15 mA compared to the 2.07 mA of WO$_{3−x}$ at 1.23 V, and the charge density from the MS plot reduced from ~ 2.31 × 10^{22} to 6.70 × 10^{21} cm^{-3}
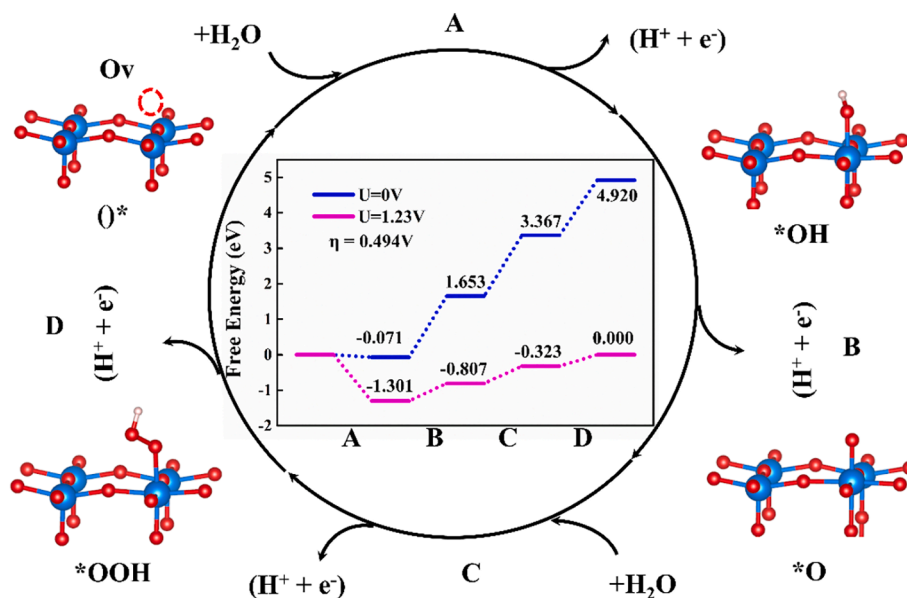
Fig. 6. OER and cumulative reaction energies on the WO_{3-x} surface terminated with W-O-W.

(Fig. 4i) lower than that of WO_{3-x}. This indicates that there were few bulk O_v in the original WO_{3-x} near to WO_3, consistent with the results of Raman spectra in Fig. 1i, and the enhanced PEC performance is attributed to the surface O_v.

3.5. DFT calculations of the OER

DFT + U simulations were applied to investigate the change in the reaction energy of the OER because of the surface O_v. The OER is a four-proton transfer process, and the free energy change of each step can be calculated by Eq. (5) with ZPE and entropy corrections, as explained in Section 2.4. The corrected free energies of the gaseous molecules are listed in Table S6. It is assumed that the initial WO_3 surface, fully terminated with oxygens, corresponds to the *O intermediate without exposed W reactive sites [56]. Therefore, water oxidation initiates from reaction C to form HOO* with the dissociation of H_2O and a proton transfer to the electrolyte, as shown in Fig. 5. Subsequently, molecular oxygen desorbs from the slab with a proton into the electrolyte, leaving an undercoordinated W atom. The undercoordinated W acts as a reactive site to dissociate water molecules forming HO*. Finally, a proton separates from the surface turning into the starting *O in a continuous catalytic cycle. The cumulative reaction energies follow the reaction process C-D-A-B for WO_3 as shown in the center of Fig. 5, with the corrected free energies shown in Table S7. The dissociation of a proton from HO* (step B) owns the maximum free energy change of 2.267 eV under no applied external potential (U = 0 V). The overall reaction energy is 0 eV for an applied potential of 1.23 V, and the overpotential (η) of the OER is 1.037 V, corresponding to step B, following Eq. (7) [57]:

$$\eta = \frac{\max(\Delta G_A, \Delta G_B, \Delta G_C, \Delta G_D)}{e} - 1.23 \qquad (7)$$

where ΔG_A, ΔG_B, ΔG_C, and ΔG_D are the free energy changes for reactions A-D calculated from Eq. (5), respectively.

EG may remove all the diagonal oxygens from the outermost layer, yielding a stable slab terminated with W-O-W as shown in Figure S4. The OER of WO_{3-x} proceeds with the reaction pathway A-B-C-D, as shown in Fig. 6, owing to the undercoordinated W active sites introduced with the O_v; it begins with water dissociation on ()* with the corrected free energy (Table S8). A proton dissociating from HO* has the highest energy change without an applied bias, similar to WO_3, with a ΔG of 1.724 eV

[58]. The overpotential is 0.494 V with the application of 1.23 V for the maximum change in step B from Eq. (5). In comparison, the η of WO_{3-x} is much lower than that of WO_3 (1.037 V), consistent with the Tafel curves (Fig. 4f), and suggests superior surface reaction kinetics from the increase in $\eta_{surface}$ with O_v [57]. These DFT calculations provide a rational basis for the high performance of O_v in experiments and why the O_v have a dramatically positive effect on the activity of WO_3 for water splitting.

4. Conclusion

We have proposed a novel method of that uses thermal reduction by EG at 130 °C to controllably introduce an appropriate number of O_v on the WO_{3-x} surface. The in-situ surface O_v are generated through bidentate hydrogen bonds, which are caused by the matched distances between alcoholic hydrogens of EG and the diagonal oxygens of the WO_3 surface without deep defects (bulk O_v). The synthesized WO_{3-x} nanoplates photoanode had a superior photocurrent density from the reduced interfacial holes-to-water resistance and the twice increase of injection efficiency compared to that of WO_3. Therefore, according to calculations and experiments, modulated surface O_v can enhance the surface kinetics by lowering the OER overpotential to improve the PEC performance.

Declaration of Competing Interest

The authors declare that they have no known competing financial interests or personal relationships that could have appeared to influence the work reported in this paper.

Appendix A. Supplementary data

Supplementary data to this article can be found online at https://doi.org/10.1016/j.cej.2020.127089.

References

[1] X. Chen, Z. Zhang, L. Chi, A.K. Nair, W. Shangguan, Z. Jiang, Recent advances in visible-light-driven photoelectrochemical water splitting: catalyst nanostructures and reaction systems, Nano-Micro Lett. 8 (2016) 1–12.

[2] A. Fujishima, K. Honda, Electrochemical photolysis of water at a semiconductor electrode, Nature 238 (1972) 37–38.

[3] S. Chen, Q. Zeng, J. Bai, J. Li, L. Li, L. Xia, B. Zhou, Preparation of hematite with an ultrathin iron titanate layer via an in situ reaction and its stable, long-lived, and excellent photoelectrochemical performance, Appl. Catal. B: Environ. 218 (2017) 690–699.

[4] S. Chen, J. Li, J. Bai, L. Xia, Y. Zhang, L. Li, Q. Xu, B. Zhou, Electron blocking and hole extraction by a dual-function layer for hematite with enhanced photoelectrocatalytic performance, Appl. Catal. B-Environ. 237 (2018) 175–184.

[5] L. Xia, J. Li, J. Bai, L. Li, S. Chen, B. Zhou, BiVO₄ photoanode with exposed (040) facets for enhanced photoelectrochemical performance, Nano-Micro Lett. 10 (2018) 11.

[6] R. Wang, J. Bai, Y. Li, Q. Zeng, J. Li, B. Zhou, BiVO₄/TiO₂(N₂) nanotubes heterojunction photoanode for highly efficient photoelectrocatalytic applications, Nano-Micro Lett. 9 (2016) 14.

[7] B. Zhang, F. Wang, C. Zhu, Q. Li, J. Song, M. Zheng, L. Ma, W. Shen, A facile self-assembly synthesis of hexagonal ZnO nanosheet films and their photoelectrochemical properties, Nano-Micro Lett. 8 (2016) 137–142.

[8] M. Li, X. Tu, Y. Wang, Y. Su, J. Hu, B. Cai, J. Lu, Z. Yang, Y. Zhang, Highly enhanced visible-light-driven photoelectrochemical performance of ZnO-modified In₂S₃ nanosheet arrays by atomic layer deposition, Nano-Micro Lett. 10 (2018) 45.

[9] X. Liu, F. Wang, Q. Wang, Nanostructure-based WO₃ photoanodes for photoelectrochemical water splitting, Phys. Chem. Chem. Phys. 14 (2012) 7894–7911.

[10] Q. Mi, A. Zhanaidarova, B.S. Brunschwig, H.B. Gray, N.S. Lewis, A quantitative assessment of the competition between water and anion oxidation at WO₃ photoanodes in acidic aqueous electrolytes, Energy Environ. Sci. 5 (2012) 5694–5700.

[11] C.A. Bignozzi, S. Caramori, V. Cristino, R. Argazzi, L. Meda, A. Tacca, Nanostructured photoelectrodes based on WO₃: applications to photooxidation of aqueous electrolytes, Chem. Soc. Rev. 42 (2013) 2228–2246.

[12] S.S. Kalanur, Y.J. Hwang, S.Y. Chae, O.S. Joo, Facile growth of aligned WO₃ nanorods on FTO substrate for enhanced photoanodic water oxidation activity, J. Mater. Chem. A 1 (2013) 3479–3488.

[13] X. Wei, Z. Wen, Y. Liu, N. Zhai, A. Wei, K. Feng, G. Yuan, J. Zhong, Y. Qiang, X. Sun, Hybridized mechanical and solar energy-driven self-powered hydrogen production, Nano-Micro Lett. 12 (2020) 88.

[14] J.C. Hill, K.-S. Choi, Effect of electrolytes on the selectivity and stability of n-type WO₃ photoelectrodes for use in solar water oxidation, J. Phys. Chem. C 116 (2012) 7612–7620.

[15] K. Fuku, N. Wang, Y. Miseki, T. Funaki, K. Sayama, Photoelectrochemical reaction for the efficient production of hydrogen and high-value-added oxidation reagents, ChemSusChem 8 (2015) 1593–1600.

[16] G. Wang, Y. Yang, D. Han, Y. Li, Oxygen defective metal oxides for energy conversion and storage, Nano Today 13 (2017) 23–39.

[17] J. Yan, T. Wang, G. Wu, W. Dai, N. Guan, L. Li, J. Gong, Tungsten oxide single crystal nanosheets for enhanced multichannel solar light harvesting, Adv. Mater. 27 (2015) 1580–1586.

[18] F. Zhan, Y. Liu, K. Wang, X. Yang, M. Liu, X. Qiu, J. Li, W. Li, Oxygen-deficient nanofiber WO₃ₓ/WO₃ homojunction photoanodes synthesized via a novel metal self-reducing method, ACS Appl. Mater. Interf. 11 (2019) 39951–39960.

[19] W. Li, P. Da, Y. Zhang, Y. Wang, X. Lin, X. Gong, G. Zheng, WO₃ nanoflakes for enhanced photoelectrochemical conversion, ACS Nano 8 (2014) 11770–11777.

[20] S.S. Kalanur, I.-H. Yoo, I.-S. Cho, H. Seo, Effect of oxygen vacancies on the band edge properties of WO₃ producing enhanced photocurrents, Electrochim. Acta 296 (2019) 517–527.

[21] J. Hu, X. Zhao, W. Chen, H. Su, Z. Chen, Theoretical insight into the mechanism of photoelectrochemical oxygen evolution reaction on BiVO₄ anode with oxygen vacancy, J. Phys. Chem. C 121 (2017) 18702–18709.

[22] X. Yao, D. Wang, X. Zhao, S. Ma, P.S. Bassi, G. Yang, W. Chen, Z. Chen, T. Sritharan, Scale-up of BiVO₄ photoanode for water splitting in a photoelectrochemical cell: issues and challenges, Energy Technol. 6 (2018) 100–109.

[23] G. Wang, Y. Ling, H. Wang, X. Yang, C. Wang, J.Z. Zhang, Y. Li, Hydrogen-treated WO₃ nanoflakes show enhanced photostability, Energy Environ. Sci. 5 (2012) 6180–6187.

[24] Y. Wang, J. Cai, M. Wu, J. Chen, W. Zhao, Y. Tian, T. Ding, J. Zhang, Z. Jiang, X. Li, Rational construction of oxygen vacancies onto tungsten trioxide to improve visible light photocatalytic water oxidation reaction, Appl. Catal. B-Environ. 239 (2018) 398–407.

[25] M. Ma, K. Zhang, P. Li, M.S. Jung, M.J. Jeong, J.H. Park, Dual Oxygen and tungsten vacancies on a WO₃ photoanode for enhanced water oxidation, Angew. Chem. Int. Ed. 55 (2016) 11819–11823.

[26] X. Zhao, J. Hu, X. Yao, S. Chen, Z. Chen, Clarifying the roles of oxygen vacancy in W-doped BiVO₄ for solar water splitting, ACS Appl. Energy Mater. 1 (7) (2018) 3410–3419.

[27] M. Ye, J. Gong, Y. Lai, C. Lin, Z. Lin, High-efficiency photoelectrocatalytic hydrogen generation enabled by palladium quantum dots-sensitized TiO₂ nanotube arrays, J. Am. Chem. Soc. 134 (2012) 15720–15723.

[28] O. Bengone, M. Alouani, P. Blöchl, J. Hugel, Implementation of the projector augmented-wave LDA+ U method: application to the electronic structure of NiO, Phys. Rev. B 62 (2000) 16392–16401.

[29] G. Kresse, J. Hafner, Ab initio molecular-dynamics simulation of the liquid-metal–amorphous-semiconductor transition in germanium, Phys. Rev. B 49 (20) (1994) 14251–14269.

[30] J.P. Perdew, K. Burke, M. Ernzerhof, Generalized gradient approximation made simple, Phys. Rev. Lett. 77 (1996) 3865–3868.

[31] Y. Wu, M.K.Y. Chan, G. Ceder, Prediction of semiconductor band edge positions in aqueous environments from first principles, Phys. Rev. B 83 (2011), 235301.

[32] K. Ulman, M.T. Nguyen, N. Seriani, R. Gebauer, Passivation of surface states of alpha-Fe₂O₃(0001) surface by deposition of Ga₂O₃ overlayers: a density functional theory study, J. Chem. Phys. 144 (2016), 094701.

[33] Y. Lv, Y. Zhu, Y. Zhu, Enhanced Photocatalytic Performance for the BiPO 4– x Nanorod Induced by Surface Oxygen Vacancy, J. Phys. Chem. C 117 (36) (2013) 18520–18528.

[34] X. Zhou, X. Zheng, B.o. Yan, T. Xu, Q. Xu, Defect engineering of two-dimensional WO 3 nanosheets for enhanced electrochromism and photoelectrochemical performance, Appl. Surface Sci. 400 (2017) 57–63.

[35] R. Zhang, C. Song, M. Kou, P. Yin, X. Jin, L.i. Wang, Y.u. Deng, B.o. Wang, D. Xia, P.K. Wong, L. Ye, Sterilization of escherichia coli by photothermal synergy of WO 3– x /C Nanosheet under infrared light irradiation, Environ. Sci. Technol. 54 (6) (2020) 3691–3701.

[36] H.-S. Kim, J.B. Cook, H. Lin, J. Ko, S. Tolbert, V. Ozolins, B. Dunn, Oxygen vacancies enhance pseudocapacitive charge storage properties of MoO3−x, Nature Mater 16 (2017) 454–460.

[37] G. Liu, J. Han, X. Zhou, L. Huang, F. Zhang, X. Wang, C. Ding, X. Zheng, H. Han, C. Li, Enhancement of visible-light-driven O2 evolution from water oxidation on WO₃ treated with hydrogen, Journal of Catalysis 307 (2013) 148–152.

[38] R. Zhang, F. Ning, S. Xu, L. Zhou, M. Shao, M. Wei, Oxygen vacancy engineering of WO₃ toward largely enhanced photoelectrochemical water splitting, Electrochimica Acta 274 (2018) 217–223.

[39] A. Naldoni, M. Allieta, S. Santangelo, M. Marelli, F. Fabbri, S. Cappelli, C. L. Bianchi, R. Psaro, V. Dal Santo, Effect of nature and location of defects on bandgap narrowing in black TiO 2 nanoparticles, J. Am. Chem. Soc. 134 (18) (2012) 7600–7603.

[40] M. Guo, J. Lu, Y. Wu, Y. Wang, M. Luo, UV and visible raman studies of oxygen vacancies in rare-earth-doped ceria, Langmuir 27 (7) (2011) 3872–3877.

[41] M.C. Paganini, L. Dall'Acqua, E. Giamello, L. Lietti, P. Forzatti, G. Busca, An EPR study of the surface chemistry of the V₂O₅–WO₃/TiO₂ catalyst: redox behaviour and state of V (IV), J. Catal. 166 (1997) 195–205.

[42] Y. Nosaka, S. Takahashi, H. Sakamoto, A.Y. Nosaka, Reaction mechanism of Cu (II)-grafted visible-light responsive TiO₂ and WO₃ photocatalysts studied by means of ESR spectroscopy and chemiluminescence photometry, J. Phys. Chem. C 115 (2011) 21283–21290.

[43] J.K. Nørskov, F. Studt, F. Abild-Pedersen, Fundamental Concepts in Heterogeneous Catalysis, Wiley, New Jersey, 2014, pp. 6–25.

[44] K. Krishnan, R.S. Krishnan, Raman and infrared spectra of ethylene glycol, Proc. Indian Acad. Sci. 64 (1966) 111.

[45] P. Buckley, P.A. Giguère, Infrared studies on rotational isomerism, I. Ethylene glycol. Can. J. Chem. 45 (1967) 397–407.

[46] P.J. Linstrom, W.G. Mallard, NIST chemistry WebBook, NIST standard reference database number 69, National Institute of Standards and Technology, Gaithersburg MD, 2014, p. 20899.

[47] F. Le Formal, S.R. Pendlebury, M. Cornuz, S.D. Tilley, M. Gratzel, J.R. Durrant, Back electron-hole recombination in hematite photoanodes for water splitting, J. Am. Chem. Soc. 136 (2014) 2564–2574.

[48] F. Le Formal, K. Sivula, M. Grätzel, The transient photocurrent and photovoltage behavior of a hematite photoanode under working conditions and the influence of surface treatments, J. Phys. Chem. C 116 (2012) 26707–26720.

[49] T.W. Kim, K.S. Choi, Nanoporous BiVO4 photoanodes with dual-layer oxygen evolution catalysts for solar water splitting, Science 343 (2014) 990–994.

[50] T. Zhou, S. Chen, L. Li, J. Wang, Y. Zhang, J. Li, J. Bai, L. Xia, Q. Xu, M. Rahim, B. Zhou, Carbon quantum dots modified anatase/rutile TiO2 photoanode with dramatically enhanced photoelectrochemical performance, Appl. Catal. B: Environ. 269 (2020) 118776.

[51] G. Liu, J. Shi, F. Zhang, Z. Chen, J. Han, C. Ding, S. Chen, Z. Wang, H. Han, C.I. Li, A Tantalum nitride photoanode modified with a hole-storage layer for highly stable solar water splitting, Angew. Chem. Int. Ed. 53 (2014) 7295–7299.

[52] F. Malara, A. Minguzzi, M. Marelli, α-Fe2O3/NiOOH: an effective heterostructure for photoelectrochemical water oxidation, ACS Catal. 5 (2015) 5292–5300.

[53] K.U. Wijayantha, S. Saremi-Yarahmadi, L.M. Peter, Kinetics of oxygen evolution at α-Fe2O3 photoanodes: a study by photoelectrochemical impedance spectroscopy, Phys. Chem. Chem. Phys. 13 (2011) 5264–5270.

[54] A. Valdes, Z.-W. Qu, G.-J. Kroes, J. Rossmeisl, J.K. Nørskov, Oxidation and photo-oxidation of water on TiO₂ surface, J. Phys. Chem. C 112 (2008) 9872–9879.

[55] S. Feng, T. Wang, B. Liu, Enriched surface oxygen vacancies of photoanodes by photoetching with enhanced charge separation, Angew. Chem. Int. Ed. 59 (2020) 2044–2048.

[56] P. Liao, J.A. Keith, E.A. Carter, Water oxidation on pure and doped hematite (0001) surfaces: prediction of Co and Ni as effective dopants for electrocatalysis, J. Am. Chem. Soc. 134 (2012) 13296–13309.

[57] Z. Wang, X. Mao, P. Chen, M. Xiao, S.A. Monny, S. Wang, M. Konarova, A. Du, L. Wang, Understanding the roles of oxygen vacancies in hematite-based photoelectrochemical processes, Angew. Chem. Int. Ed. 58 (2019) 1030–1034.

[58] Y. Liu, J. Li, H. Tang, W. Li, Y. Yang, Y. Li, Q. Chen, Enhanced photoelectrochemical performance of plate-like WO_3 induced by surface oxygen vacancies, Electrochem. Commun. 68 (2016) 81–85.